

Multi-Position RF MEMS Tunable Capacitors Using Laterally Moving Sidewalls of 3-D Micromachined Transmission Lines

Umer Shah, *Student Member, IEEE*, Mikael Sterner, and Joachim Oberhammer, *Senior Member, IEEE*

Abstract—This paper presents a novel concept of RF microelectromechanical systems (MEMS) tunable capacitors based on the lateral displacement of the sidewalls of a 3-D micromachined coplanar transmission line. The tuning of a single device is achieved in multiple discrete and well-defined tuning steps by integrated multi-stage MEMS electrostatic actuators that are embedded inside the ground layer of the transmission line. Three different design concepts, including devices with up to seven discrete tuning steps up to a tuning range of 58.6 to 144.5 fF ($C_{\max}/C_{\min} = 2.46$), have been fabricated and characterized. The highest Q factor, measured by a weakly coupled transmission-line resonator, was determined as 88 at 40 GHz and was achieved for a device concept where the mechanical suspension elements were completely de-coupled from the RF signal path. These devices have demonstrated high self-actuation robustness with self-actuation pull-in occurring at 41.5 and 47.8 dBm for mechanical spring constants of 5.8 and 27.7 N/m, respectively. Nonlinearity measurements revealed that the third-order intermodulation intercept point (IIP3) for all discrete device states is above the measurement-setup limit of 68.5 dBm for our 2.5-GHz IIP3 setup, with a dual-tone separation of 12 MHz. Based on capacitance/gap/spring measurements, the IIP3 was calculated for all states to be between 71–91 dBm. For a mechanical spring design of 5.8 N/m, the actuation and release voltages were characterized as 30.7 and 21.15 V, respectively, and the pull-in time for the actuator bouncing to drop below 8% of the gap was measured to be 140 μ s. The mechanical resonance frequencies were measured to be 5.3 and 17.2 kHz for spring constant designs of 5.8 and 27.7 N/m, respectively. Reliability characterization exceeded 1 billion cycles, even in an uncontrolled atmospheric environment, with no degradation in the pull-in/pull-out hysteresis behavior being observed over these cycling tests.

Index Terms—Micromachined transmission line, micromachining, RF microelectromechanical systems (MEMS), switched capacitor, tunable capacitor.

I. INTRODUCTION

TUNABLE capacitors form an integral part of frequency-agile microwave systems. Micromachined RF/microwave tunable devices, often referred to as RF microelectromechanical systems (MEMS), are gaining considerable interest and are

Manuscript received October 12, 2012; revised April 04, 2013; accepted April 08, 2013. Date of publication May 06, 2013; date of current version May 31, 2013.

The authors are with Micro and Nanosystems, School of Electrical Engineering, KTH Royal Institute of Technology, Stockholm SE-100 44, Sweden (e-mail: umers@kth.se; msterner@kth.se; joachim.oberhammer@ee.kth.se).

Color versions of one or more of the figures in this paper are available online at <http://ieeexplore.ieee.org>.

Digital Object Identifier 10.1109/TMTT.2013.2259499

under active development due to their superior performance when compared to their solid-state counterparts, despite recent improvements in quality factor and self-resonance frequency [1], [2], and also linearity and tuning ratio of solid-state varactor diodes [3]. MEMS tunable capacitors have shown the potential to replace solid-state varactor diodes in applications such as: 1) phase shifters [4]; 2) voltage-controlled oscillators; 3) tunable filters [5]; and 4) impedance matching networks [6] because of their ability of near-ideal signal-handling behavior, low power consumption, low loss, and large bandwidth [7]. These devices also have the ability to achieve high self-resonance frequencies [8]. In the literature, the following four different principles have been shown to implement MEMS tunable capacitors.

- 1) Tunable parallel-plate capacitors, consisting of a fixed electrode and an electrode moved by an integrated MEMS actuator, which can either be utilized in analog tuning, or as RF MEMS switched capacitors [9], [10].
- 2) Tunable interdigital capacitors, consisting of two comb-like electrode structures of which one can be moved by a MEMS actuator, can achieve better tuning linearity and a larger tuning range, but have a lower quality factor at high frequencies, lower self resonance frequencies, and occupy a larger area [11] as compared to the parallel-plate approach [8].
- 3) Switched capacitor banks [12], [13] in which MEMS switches are used to select fixed metal–insulator–metal (MIM) or metal–air–metal (MAM) capacitors out of a capacitor bank.
- 4) A fourth concept consists of changing the dielectric loading of a transmission line by moving a dielectric block [14]. The authors have recently implemented this concept for a low-loss MEMS-movable dielectric-block phase shifter [4], [15].

From a circuit point of view, digital tuning is most often preferred over analog tuning, as it provides well-defined capacitances and is robust to the actuation voltage. Whereas, analog tunable capacitors require accurate control of the actuation voltage, if not a feedback mechanism, and typically have lower linearity and a lower maximum/minimum capacitance ratio. Thus, analog tuning is typically mimicked by switched capacitor banks [12], [13].

Recently, RF MEMS-reconfigurable capacitor banks have achieved some success in commercial RF systems [16]. Sub-microsecond switching times have also been achieved by utilizing miniature capacitive beams [9], [17]. It has also been shown that using a MAM capacitor configuration, i.e., removing the

TABLE I
PERFORMANCE COMPARISON OF TUNABLE CAPACITORS

Device Technology	Capacitance ratio	Quality factor (freq.)	Switching time
MEMS [11]	8.4 : 1	35 (2 GHz)	6 ms
MEMS [8]	1.9 : 1	100 (34 GHz)	NA
MEMS [9]	2.3 : 1	50 (20 GHz)	400 ns
MEMS [10]	2 : 1	225 (X-Ku band)	8 μ s
CMOS-MEMS [20]	4.6 : 1	> 300 (1.5 GHz)	NA
MEMS [18]	3 : 1	10 (10 GHz)	NA
MEMS [21]	2.8 : 1	8.8 (1 GHz)	NA
MEMS [17]	3 : 1	90 (20 GHz)	200 ns
MEMS [19]	9 : 1	100 (C-X band)	50 μ s
MEMS [22]	20 : 1	85 (3.127 GHz)	<10 μ s
CMOS-MEMS [23]	63 : 1	160 (1 GHz)	600 μ s
CMOS [1]	1.6 : 1	> 100 (24 GHz)	NA
GaAs [3]	9 : 1	50 (2 GHz)	NA
SiC [24]	6 : 1	160 (2 GHz)	NA
CMOS [25]	7.7 : 1	35 (1 GHz)	NA
MEMS (this work)	1.48 : 1	80 (40 GHz)	140 μs

isolation layer in the MEMS actuator, results in low losses [18] and reliability improvement [10], [19].

The quality factor and tuning range are important parameters for tunable capacitors, and the most remarkable achievements reported in the literature are summarized in Table I along with the switching times, and are compared to the device introduced in this paper. A comparison between the Q factors is difficult since the Q factors drop inverse-proportionally with the frequency.

This paper presents a new concept of MEMS capacitors tunable in multiple discrete and well-defined steps, implemented by in-plane moving of the ground sidewalls of a 3-D micromachined coplanar waveguide transmission line. The MEMS actuators are completely embedded in the ground layer of the transmission line, and fabricated using a single-mask silicon-on-insulator (SOI) RF MEMS fabrication process, originally developed by the authors for switches [26]. The authors have shown basic ideas of tunable capacitors based on moving sidewalls at previous conferences [27], [28], including an attempt of building a filter on such a tuning technology [29]. This paper analyzes and compares three fundamental concepts of moveable-sidewall tunable capacitors in detail, where the tuning is achieved by: 1) Design I: bending the mechanically compliant ground sidewall; 2) Design II: single and multistage lateral movement of the ground sidewalls with the signal routed over the mechanical springs; and 3) Design III: lateral movement of the ground sidewalls with an actuation mechanism de-coupled from the RF signal path. This paper is primarily focusing on the third concept, whose evaluation data is published here for the first time, as it achieves, by far, the best performance due to de-coupled RF and MEMS-actuation functional elements. It is shown that this novel tunable-capacitor concept achieves low insertion loss, a high quality factor, high reliability, high linearity, and high self-actuation robustness, evaluated up to 40 GHz.

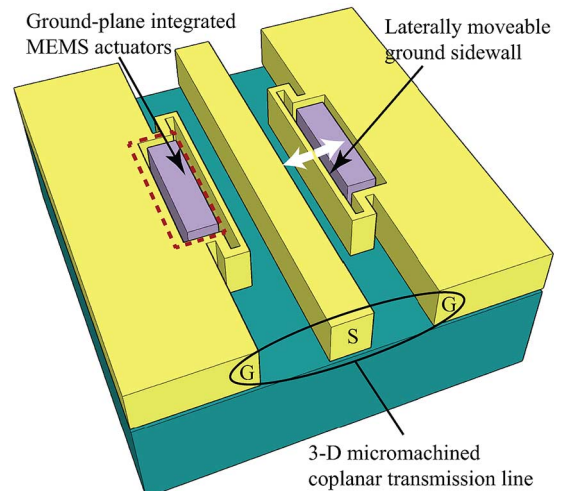


Fig. 1. Basic concept of the MEMS tunable capacitors presented in this paper, based on in-plane moveable sidewalls of the ground layer of a 3-D micromachined coplanar transmission line, displaced by integrated MEMS electrostatic actuators.

II. CONCEPT AND IMPLEMENTATIONS

The basic function of the capacitor, shown in Fig. 1, comprises the changing of the capacitive loading of a 3-D micromachined coplanar waveguide transmission line by a laterally moveable section of the ground layer sidewall, which is achieved by integrated MEMS actuators. This translates to a change of the capacitive part in the transmission-line equivalent-circuit model. The MEMS actuators are completely embedded in the ground layer of the micromachined transmission line, thereby not adding any additional discontinuity in the slots, in contrast to conventional MEMS capacitors and switches that often employ biasing lines and electrodes in the signal-to-ground gap. One of the key advantages of the proposed concept is that the tuning of the capacitors is done in multiple well-defined discrete tuning steps, which unifies the advantages of analog tuning (high resolution between minimum and maximum capacitance) and digital tuning (well-defined capacitances without feedback mechanism, actuation voltage robustness, high linearity, self-actuation robustness), even for a single device, i.e., without requiring area-consuming capacitor banks. This is achieved by stacking multiple actuators, which also offers the benefit of extended tuning range, actuating both sides alone for asymmetrical operation, creating intermediate overall capacitance steps. Such a slight asymmetry does not result in significant line imbalance, which was verified by mode analysis, neither do the measurement indicate any unexpected behavior. The tuned RF capacitor is composed of a pure MAM geometry that avoids dielectric charging. The actuation mechanism is also based on an all-metal design, i.e., the actuators do not require any dielectric layers that are prone to dielectric charging, and thus decrease reliability and actuation voltage repeatability [30]. Instead, stoppers are used to avoid actuation-electrode short circuit. A further reliability-enhancing feature of the design is the utilization of monocrystalline silicon as the core-structural material for all moving parts, which is then metallized. As the metallization is symmetrical on the

TABLE II
OVERVIEW OF THE ADVANTAGES AND DISADVANTAGES OF THE THREE DESIGN CONCEPTS

Advantages common to Design I, Design II and Design III			
Advantages	<ul style="list-style-type: none"> • Multi-step digital tuning. • Accurately defined and reproducible tuning states. • 3-D MEMS transmission line (metal covered silicon core with decreased dielectric losses). • Actuator embedded in ground layer (actuation elements are invisible to wave propagation). • All metal design (no dielectric layer between actuator and electrode; no charging). • Metallized silicon core (high reliability, temperature compensation). • No need for DC bias on the signal line. • Single mask fabrication process. 		
Additional advantages individual to Design I, Design II and Design III			
Design I	Design II	Design III	
Advantages	<ul style="list-style-type: none"> • Extended tuning range by stacking actuator stages. • Number of states independent of required transmission line length. 	<ul style="list-style-type: none"> • Extended tuning range by stacking actuator stages. • Number of states independent of required transmission line length. • Mechanical suspension is decoupled in its function from the RF signal path. • DC ground not shared with RF ground, i.e. de-coupled RF and DC potentials. • High self actuation robustness. • High reliability. • High linearity. • High Q-factor. 	
Disadvantages individual to Design I, Design II and Design III			
Design I	Design II	Design III	
Disadvantages	<ul style="list-style-type: none"> • Low capacitance ratio due to bending and not displacement of the capacitive element. 	<ul style="list-style-type: none"> • Increased loss due to RF signal routing via mechanical springs. • Low Q-factor. 	

sidewalls, the devices are to a large extent temperature compensated by design. In contrast to many conventional MEMS tunable capacitors, the signal line of the transmission line is not used for dc biasing the actuation mechanism. For two of the three presented design concepts, the RF ground shares the same potential as the dc ground and the dc biasing occurs on electrodes outside the RF signal path. For the third design, even the dc ground is decoupled from the RF ground. Furthermore, a benefit of 3-D micromachined transmission lines is reduced substrate losses, as the electric field lines are mainly confined to the free space above the substrate, resulting in low overall insertion loss [31]. The fabrication of these laterally moving SOI RF MEMS devices is simple, as all transmission line and tuning elements are fabricated using a single photolithographical step.

Three different designs, exploring different ways of moving the ground layer sidewalls, have been implemented for this novel tunable capacitor concept, and are introduced in Sections II-A–II-C. Furthermore, Table II lists the general advantages and disadvantages of the three different design implementations. In general, it should be noted that the capacitance values and the tuning range are higher for 3-D micromachined transmission lines with sidewall metallization, but the Q factor is lower as compared to 3-D micromachined transmission lines with top metallization only, i.e., planar transmission lines suspended above the substrate. The self-resonance frequency of the devices is dependent on the length of the device. By increasing the length of the device, both the inductance and capacitance increases, thus reducing the self-resonance frequency.

A. Design I: Tuning by Bending the Ground Sidewall

Fig. 2 shows a 3-D sketch of this tunable capacitor concept. This design uses a 3-D transmission line (signal line width, gap, height = $80\ \mu\text{m}$, $90\ \mu\text{m}$, and $30.5\ \mu\text{m}$) where the sidewalls are also covered by metal, thereby forming a parallel-plate capacitor to the ground with a relatively low fringing-field part (plate height: $30.5\ \mu\text{m}$; gap: $2\ \mu\text{m}$ nonactuated, $4\ \mu\text{m}$ in the central part when actuated; length: $600\ \mu\text{m}$; thickness: $5\ \mu\text{m}$). The tuning is achieved by bending of the compliant sidewall with an electrostatic actuator, by applying a dc voltage between the actuation electrode and ground plane. In principal, analog tuning is possible, but the presented designs were operated as switched capacitors, i.e., the capacitive element pulls in until touching the stoppers, which are in place to avoid any short circuit between the electrode and actuator. As a tunable sidewall is arranged on each side of the signal line, the tunable capacitor has a total of three different states. For this device concept, only a low capacitance ratio can be achieved as the ground sidewall is not deflected over its whole length, and as it is more difficult to stack actuators for multiple discrete steps as compared to the other tuning concepts. The fabricated prototype device shown in Fig. 3 had an overall transmission line length of $820\ \mu\text{m}$ including the probe pads.

B. Design II: Lateral Movement of Ground Sidewall With Signal Routing Over Mechanical Springs

For Design II, the ground sidewall section is moved uniformly over its entire length, and the mechanical compliance

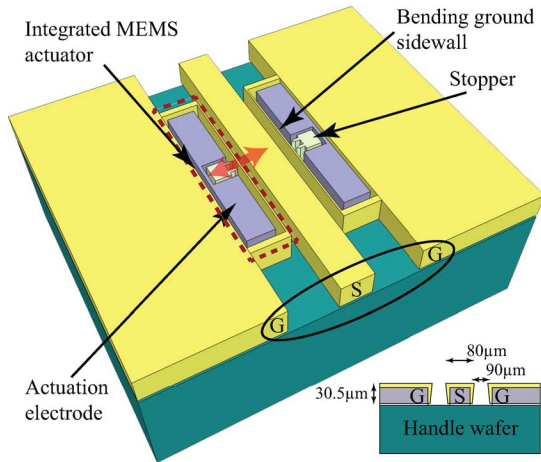


Fig. 2. Design I: 3-D illustration of ground sidewall integrated tunable capacitor with bending sidewalls.

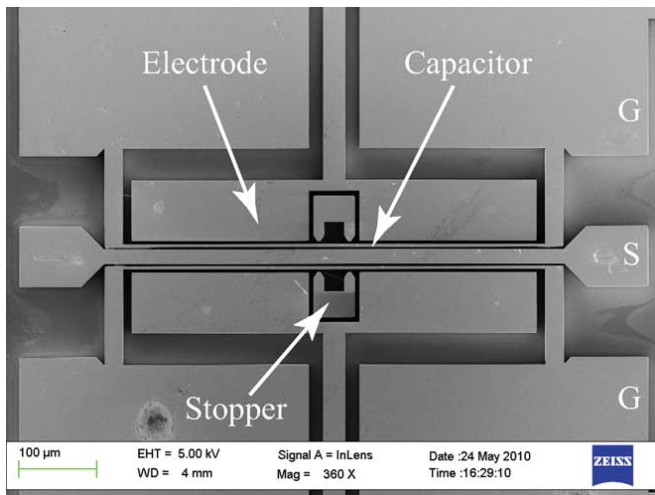


Fig. 3. SEM photograph of fabricated prototype tunable capacitors of Design I.

is achieved by additional mechanical springs, as shown in the 3-D drawing in Fig. 4. This design also utilizes 3-D transmission lines (signal line width, gap, height = $80\ \mu\text{m}$, $90\ \mu\text{m}$, $30.5\ \mu\text{m}$) with metal coverage on the sidewalls forming the capacitor (plate height: $30.5\ \mu\text{m}$; gap: $6\ \mu\text{m}$ nonactuated, $2\ \mu\text{m}$ when all stages are actuated; length: $600\ \mu\text{m}$; movable sidewall width: $20\ \mu\text{m}$; spring thickness: $5\ \mu\text{m}$). As the moveable sidewalls are connected to the ground plane via mechanical springs, the RF ground signal is also routed via the folded springs, which results in limited RF performance due to the increased overall series resistance of the capacitor. This design concept with uniformly moving sidewalls allows for lateral stacking of actuator stages, which results in larger sidewall movement, i.e., an extended tuning range, in accurately defined discrete steps for each actuation stage. The increased displacement can be achieved at medium actuation voltages as the total movement is split in smaller parts through sequential operation of the actuators, as shown in Fig. 5 for a two-stage design. For actuating a subsequent stage, all the previous stages have to be actuated. Thus, in contrast to a conventional switched capacitor, this concept allows multiple states. In addition to the multi-states achieved

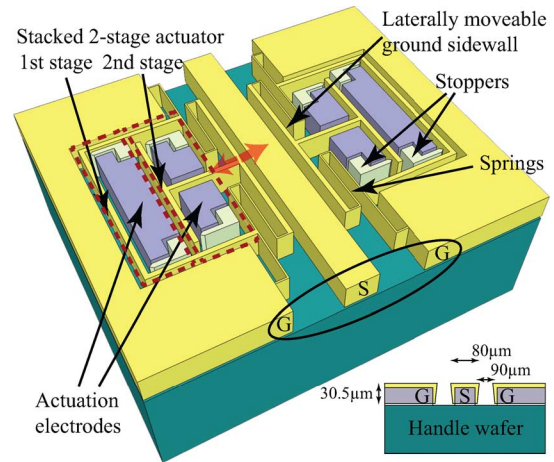


Fig. 4. Design II: 3-D illustration of ground sidewall integrated tunable capacitor with sidewalls displaced uniformly over their entire length, shown for a two-stage actuator achieving five discrete tuning steps.

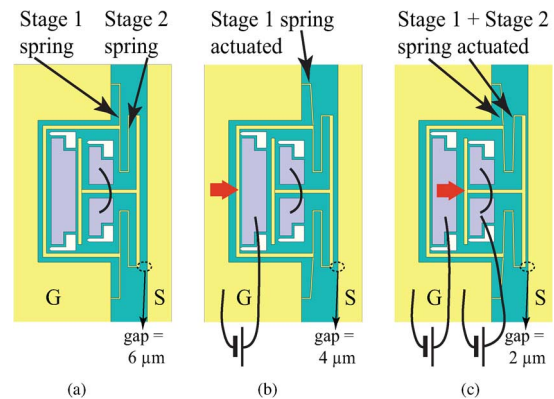
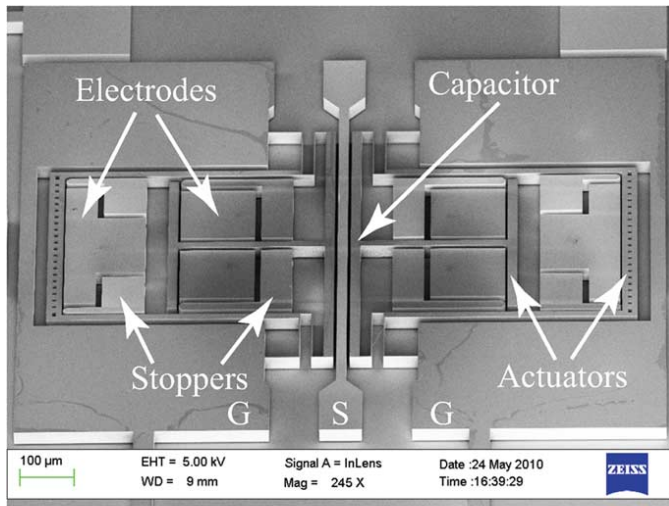


Fig. 5. Actuation states of a two-stage Design II capacitor (only one side of the coplanar transmission line illustrated). (a) Unactuated. (b) Stage 1 actuated (half displacement). (c) Stage 2 in addition to stage 1 actuated (full displacement).

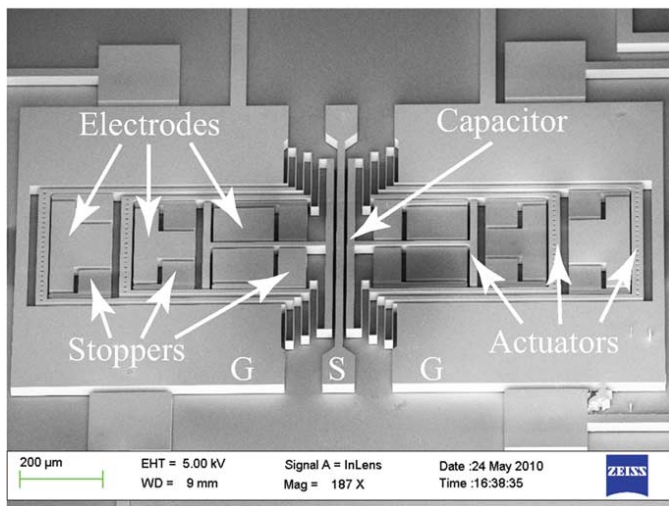
by multi-stage actuators, this concept offers additional capacitance states as the device can be actuated asymmetrically, i.e., each side of the symmetrically duplicated design can be actuated independently. In total, a number of $2n - 1$ states can be achieved with n being the number of single-side actuation stages. It should be noted that the length of the tunable capacitor, and thus its insertion loss, is independent of the number of actuation stages, which is a unique property for a digitally controlled tunable capacitor. SEM photographs of implementations with two- and three-stage actuators, resulting in five and seven capacitance states, respectively, are shown in Fig. 6 with an overall transmission line length of 1 mm including the probe pads.

C. Design III: Lateral Movement of Ground Sidewall With Additional Capacitive Coupling to Ground

The major disadvantage of Design II is that the RF signal is routed via the thin and long mechanical springs, increasing the overall insertion loss. In Design III, shown in Fig. 7, the mechanical springs are completely decoupled from the RF signal, i.e., the RF ground signal is coupled capacitively from the fixed



(a)



(b)

Fig. 6. SEM photographs of fabricated prototype tunable capacitors of Design II. (a) Implementation with two-stage actuator (five discrete tuning states). (b) Implementation with three-stage actuator (seven discrete tuning states).

ground layer to the moving ground sidewall, and the mechanical springs are connected to isolated islands behind the moving sidewalls. This results in much reduced series resistance, and thus lower insertion loss and higher Q_c of the tunable capacitor as compared to the Designs II. The mechanical spring length and thus stiffness and actuation voltage can then be designed without implications on the RF performance. For the prototypes evaluated in this paper, the 3-D transmission line of Design III is implemented with top metallization only (signal line width, gap, suspension height = $130\ \mu\text{m}$, $130\ \mu\text{m}$, $30\ \mu\text{m}$), as it was found that the transmission lines of Designs I and II had higher losses due to their relatively thin metallization layer on the sidewalls. Thus, this 3-D micromachined transmission-line implementation rather comprises a planar transmission line suspended above the substrate for reducing the substrate losses [32], [33]. With top metallization only, the overall capacitance is dominated by fringing field components, which results in a lower overall capacitance and capacitance ratio as compared

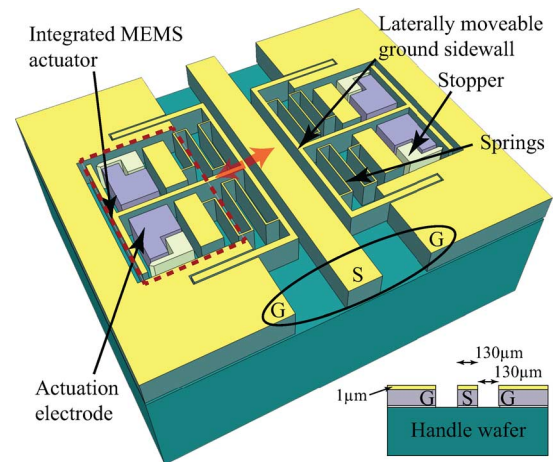


Fig. 7. Design III: 3-D illustration of ground sidewall integrated tunable capacitor with ground capacitive coupling, completely de-coupling the mechanical from the RF functional elements. This design concept achieves best performance of all the presented moving-sidewall tunable-capacitor concepts, and is therefore most extensively investigated in this paper.

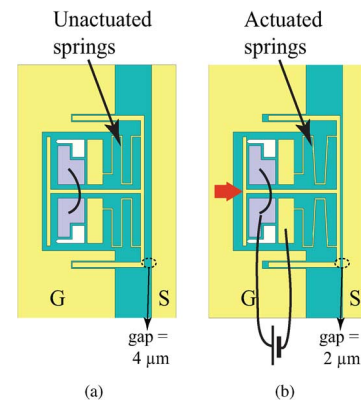


Fig. 8. Actuation states of a Design-III tunable capacitor implemented with a single-stage actuator (only one side of the coplanar transmission line is illustrated). (a) Unactuated. (b) Actuated.

to an implementation with sidewall metallization. Fig. 8 shows the actuation principle of a Design-III tunable capacitor with a single-stage actuator. The device is actuated by applying a voltage between the actuation electrode and the anchors connected to the springs, i.e., in contrast to Designs I and II, no dc bias or reference ground is shared with any RF potential, neither the RF ground, nor the signal line. More stages can also be integrated for this design as is done for Design II, resulting in additional states of the capacitor and extended tuning range. The fabricated prototype Design III is shown in Fig. 9.

III. FABRICATION

All structures are fabricated in a single-mask SOI RF MEMS process developed by the authors and outlined in Fig. 10. A high-resistivity $>3000\ \Omega \cdot \text{cm}$ SOI wafer is used with a device layer thickness of $30\ \mu\text{m}$, a buried oxide layer of $3\ \mu\text{m}$, and a handle wafer thickness of $500\ \mu\text{m}$ [see Fig. 10(a)]. First, the SOI device layer is structured by deep reactive ion plasma etching (DRIE) [see Fig. 10(b)], followed by free etching of the moving structures by wet etching of the buried oxide layer using hydrofluoric acid [see Fig. 10(c)]. A $0.5\text{-}\mu\text{m}$ -thick layer of gold is

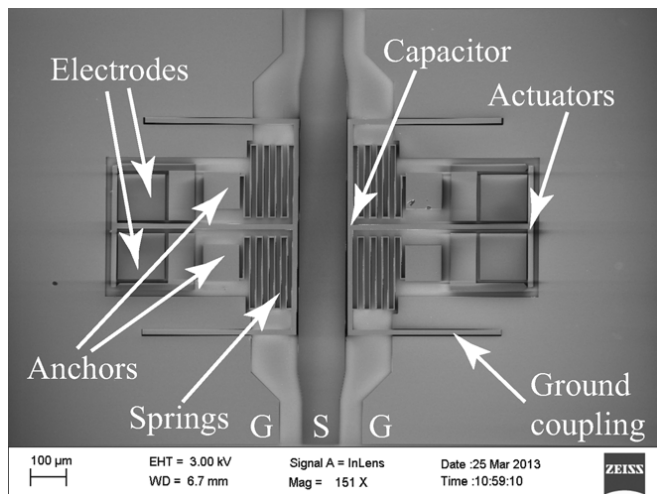


Fig. 9. SEM photograph of fabricated prototype tunable capacitor of Design III with single-stage MEMS actuator (three tuning states).

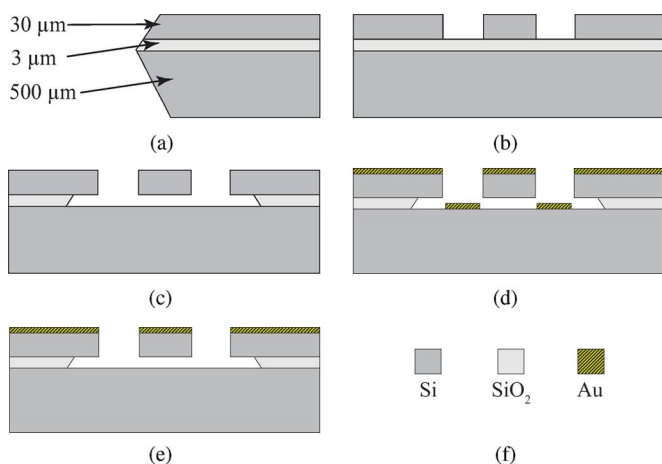


Fig. 10. SOI RF MEMS fabrication process of the tunable capacitors [26]. (a) SOI wafer. (b) Deep reactive ion etching (DRIE) of the device layer. (c) Free etching of the moving structures by HF wet etching the buried oxide layer. (d) Metallization by high-directivity e-beam evaporation. (e) Etching of unwanted metal areas by electrochemically assisted selective etching of gold.

sputtered on the wafer using 50 nm of titanium tungsten as adhesion layer for the prototypes of Design I and Design II. The sidewall metallization thickness is as small as 50 nm, in particular for smaller openings including the capacitor gap. The sidewall thickness could, in principle, be improved by using electroplating or electroless plating. However, plating would not work for the narrow gaps and high aspect ratios employed in these designs, which results in large plating nonuniformities. For the prototypes of Design III, a 1- μm -thick layer of gold on a 50-nm titanium as an adhesion layer is evaporated using high-directivity e-beam evaporation to achieve top-metallization only [see Fig. 10(d)]. Finally, the metal coating on the substrate and in the unwanted areas (for instance, in the gap between the signal and ground layer of the coplanar transmission line) is removed by electrochemically assisted selective etching of gold [34] in an electrically biased potassium iodide and sodium sulfite solution [35] [see Fig. 10(e)]. All the above wet steps are followed by a critical point drying step.

TABLE III
PERFORMANCE SUMMARY OF REPRESENTATIVE PROTOTYPE
IMPLEMENTATIONS OF THE THREE DESIGNS

Parameter	Design I	Design II	Design III
Q (40 GHz)	3	$3.8^a/3.6^b$	88^c
C_{\max} (fF)	127	$144.5^a/134^b$	60
C_{\min} (fF)	104	$58.6^a/57^b$	40.53
C_{\max}/C_{\min}	1.22	$2.46^a/2.35^b$	1.48
Number of states	3	$5^a/7^b$	3
Mechanical resonance frequency (kHz)	-	-	$5.3^d/17.2^e$
Pull-in time (μs)	-	-	140
Self actuation pull-in (dBm)	-	-	$41.5^d/47.8^e$
IIP3 (dBm)	-	-	> 68.5
Reliability (cycles)	-	-	$> 10^9$
Device length (μm)	600	600	600
SRF (GHz)	f	f	46

^aDevice with two stage actuators, derived from S-parameters

^bDevice with three stage actuators, derived from S-parameters

^cDerived using transmission line resonator

^d $k = 5.8$ N/m

^e $k = 27.7$ N/m

^fNot evaluated due to low Q factor

IV. MEASUREMENTS

Both the RF performance and MEMS actuator performance of the tunable capacitors of all designs were characterized. The RF measurements of the fabricated capacitors were performed using an Agilent E8361A PNA vector network analyzer calibrated using a GGB Industries CS-5 calibration standard and 150- μm ground-signal-ground (GSG) coplanar probes and short-open-load-thru (SOLT) calibration. Table III shows the performance summary of the three designs, discussed in detail in Sections IV-A–IV-C.3.

A. Characterization of Design I

Fig. 11 show the total insertion and return loss of the actuated and nonactuated states for Design I, compared to the insertion loss of a transmission line of the same length without a tunable capacitor. The loss of the 3-D micromachined transmission line alone is 1.17 dB at 20 GHz, attributed to the poor sidewall metal coverage of the fabricated prototypes. For the capacitors of Design I, the insertion loss is 1.61 dB in the actuated state and 2.07 dB in the unactuated state at 20 GHz, of which the transmission line alone contributes by 1.17 dB. The capacitance is extracted from the S-parameters by first de-embedding the probe pads and the transmission line using the procedure provided in [36]. The capacitance is then extracted by making the assumption of an equivalent T-network with a central capacitor corresponding to the 600- μm -long distributed capacitor element. This corresponds to a transformation of a series of pi-networks (distributed capacitor) to an equivalent single T-network. The capacitance derived by this method from the measured S-parameters deviates from the stated values by less than 1.3% from

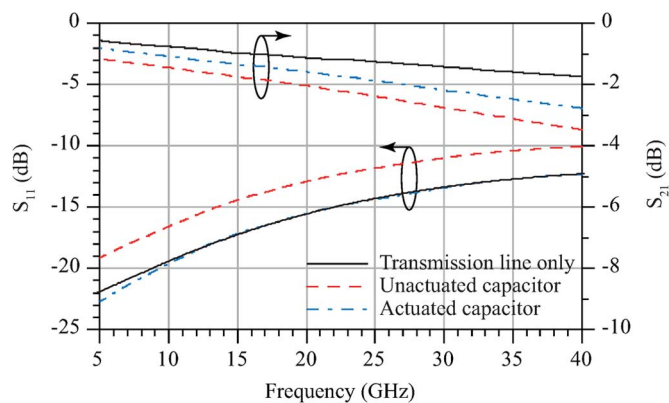


Fig. 11. Measured S -parameters for fabricated prototype of Design I.

5 to 35 GHz. The extracted capacitance is 127 fF in the nonactuated state and 104 fF in the actuated state, resulting in a capacitance ratio of 1.22. This measured capacitance ratio is low because the capacitive element is only bending when it is actuated and not displaced over its entire length as for Design II and III. The actuation voltage was determined by measurements to 40 V for a spring constant of 21.2 N/m and 110 V for a spring constant of 66 N/m.

B. Characterization of Design II

Fig. 12(a) and (b) shows the insertion and return loss of devices of Design II with two and three actuation stages, respectively, in their various actuation states. Table IV lists all states of a two- and three-stage tunable capacitor with the capacitances extracted from S -parameter measurements using de-embedding techniques [36] and the procedure described for Design I. The two-stage device can be operated in five discrete steps with a tuning range from 58.6 to 144.5 fF, which corresponds to a C_{\max}/C_{\min} of 2.46, and the three-stage device with a total of seven discrete steps can be tuned from 57 to 134 fF (C_{\max}/C_{\min} of 2.35). The capacitance ratio is much higher than for Design I, as the sidewalls in Design II are laterally moved over their entire length in contrast to bending for Design I, and due to the larger total traveling distance of 4 μm since the total movement is split into a number of smaller steps completed by successive actuators. Design II thus results in multiple, accurately defined, and reproducible tuning states. The gap between the laterally moved ground-plane sidewall and the rigid signal line is 2 and 6 μm in the two extreme positions. For actuating of a higher order stage, all previous stages already have to be pulled in. Different actuators with varying spring constants have been designed, fabricated, and evaluated with the actuation voltage of two-stage actuators ranging from 24 V (10.3-N/m spring constant) to 74 V (95 N/m) for stage 1 and 15 V (3.48 N/m) to 53 V (45.3 N/m) for stage 2. The three-stage actuation voltage ranges from 23 V (22.5 N/m) to 72 V (211 N/m) for stage 1, 19 V (12.7 N/m) to 53 V (94 N/m) for stage 2, and 18 V (9.5 N/m) to 50 V (73.2 N/m) for stage 3. Higher losses are expected for Design II as compared to Design I because of the longer RF ground path length, as the RF ground signal is routed over the mechanical springs of the multi-stage actuators.

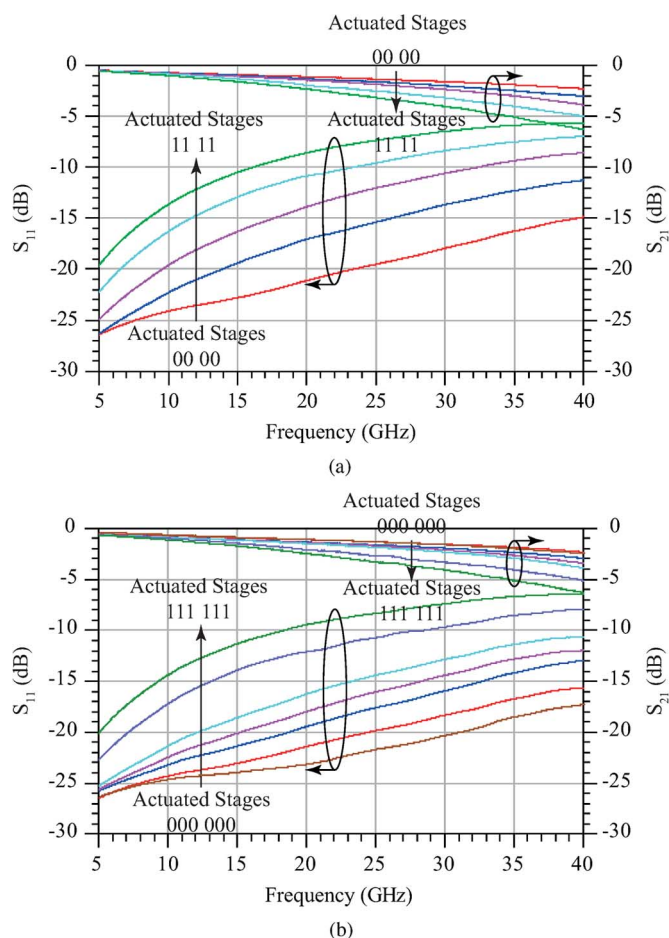


Fig. 12. Measured S -parameters of prototype devices of Design II. (a) Device with two-stage actuator (five tuning states). (b) Device with three-stage actuator (seven tuning states). (The capacitances corresponding to the states are listed in Table IV).

TABLE IV
DESIGN II: ACTUATION STATES WITH CAPACITANCES EXTRACTED FROM S -PARAMETER MEASUREMENTS FOR TWO-STAGE AND THREE-STAGE ACTUATORS

Actuator	Actuated Stages (left) 12 21 (right)	Measured Capacitance (fF)
Two stage	00 00	58.6
	10 00	67.3
	10 01	87.1
	11 01	114.2
	11 11	144.5
Actuator	Actuated Stages (left) 123 321 (right)	Measured Capacitance (fF)
Three stage	000 000	57
	100 000	57
	100 001	58.6
	110 001	61
	110 011	69.3
	111 011	100.4
	111 111	134

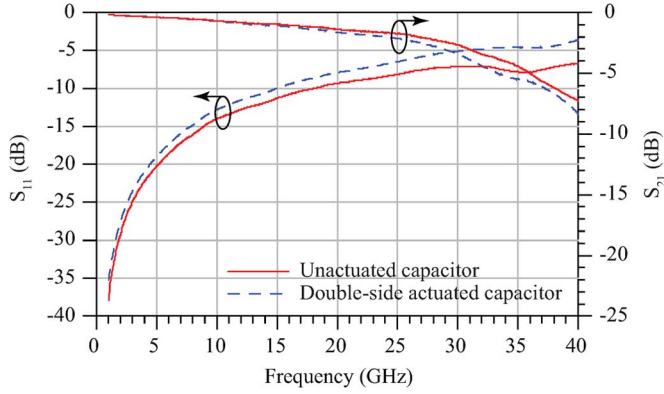


Fig. 13. Measured S -parameters for fabricated prototype of Design III for the unactuated and symmetrically actuated states.

C. Characterization of Design III

Design III has the overall best performance of all implemented design concepts and is therefore investigated in more detail. The fabricated devices have an overall transmission line length of 1.2 mm including the probe pads. The length of the moving sidewall is 600 μm , the moving sidewall and the moving electrode of the coupling capacitor are 15 μm wide, and the length of the coupling capacitor is 200 μm . The top metallization thickness is 1- μm gold. The initial, i.e., unactuated, gap of the tunable capacitor is 4 μm , closing to 2 μm in the actuated state.

1) *RF Characterization*: The prototype devices have been implemented only with single-stage actuators and thus can be operated in three discrete tuning states. As described before, more stages can be designed to achieve more tuning steps, similar to Design II. Fig. 13 shows the insertion and return loss for Design III for the unactuated and all-actuated capacitor states. A de-embedding technique [36] was used to de-embed the transmission line and the probe pads for extracting the capacitance values using the procedure described for Design I and Design II. The capacitance can be tuned from 40.53 fF in the unactuated state to 60 fF in the double-side actuated state in three steps, resulting in a capacitance ratio ($C_{\text{max}}/C_{\text{min}}$) of 1.48. This capacitance ratio is lower than reported for Design II, as the overall capacitance is dominated by the fringing field in this top-metallization-only implementation. The design has the potential for improved capacitance ratio, which largely depends on the traveling distance of the moving sidewall. Thus, the tuning ratio can be increased by adding multiple stages, as shown for Design II. For all three design concepts, the capacitance ratio could further be improved by moving the sidewall closer to the signal line than the implemented 2 μm . The losses of the prototypes of Design III are much lower than for Design I and II, since for Design III, the mechanical springs are completely isolated from the RF signal and they are no longer used for signal routing, thereby reducing the total series resistance. Fig. 14 shows the capacitance extracted from the measured S -parameters compared to the capacitances extracted from the HFSS-simulated S -parameters. The third (intermediate) capacitance value is achieved for asymmetrical operation, i.e., when only one side is actuated. For comparison, Fig. 14 also shows the interpolation curves of

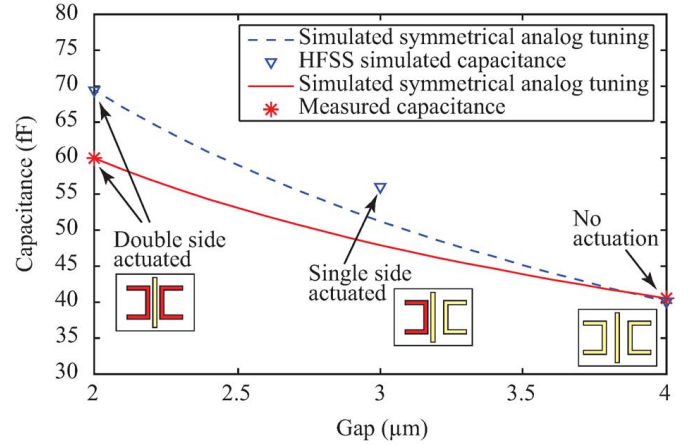


Fig. 14. Measured capacitances for fabricated prototype of Design III, compared to the HFSS-simulated discrete states, fitted by COMSOL Multiphysics simulated capacitance curves assuming gradually displaced sidewalls between the minimum and maximum positions.

the capacitances for fully analog tuning, simulated with Comsol Multiphysics, and fitted to both the measured capacitance values and the HFSS simulated capacitances. The ground coupling capacitor for a single end of a single moving sidewall was determined as 17.63 fF, derived from HFSS simulations of structures with and without the coupling capacitors. This ground coupling series capacitor reduces the overall value of the tuning capacitance from 92.4 to 40 fF in the unactuated and from 168 to 70 fF in the all-actuated state. The capacitance tuning ratio is minimally affected by the series coupling capacitors and changes from 1.82 to 1.75. The self-resonance frequency for the prototype of Design III was observed to be 46 GHz.

A method based on loading a resonator with the capacitor is used for the determination of the Q . This is the recommended method for obtaining the Q for low-loss capacitors since the denominator in the standard S -parameter technique is very sensitive to $|S_{11}|^2$ [7]. Design III is expected to have high Q , for three reasons: firstly, because of the MAM parallel-plate capacitor configuration of the presented tunable capacitor concepts; secondly, because the mechanical springs are completely decoupled from the RF signal and thus reducing the series resistance, which is a major improvement over Design II; and thirdly, because the 3-D micromachined transmission line with thin sidewall metallization of the Designs I and II has been replaced by a suspended planar transmission line. The quality factor of the capacitor was measured using a specifically designed weakly coupled transmission-line resonator. The capacitor is placed in such a resonator with a nominal resonant frequency of 40 GHz and a known (measured) unloaded Q_r of 14.88. The loaded $Q(Q_l)$ of the resonator/capacitor combination was extracted from the measured resonance behavior of the transmission line with the capacitor using $Q_l = f_o/\Delta f$. The unloaded $Q(Q_u)$ of the combined structure is then determined by $Q_u = Q_l/(1 - |S_{21}|)$, which is equal to the loaded $Q(Q_u = Q_l)$ if $S_{21} < -20$ dB. The unloaded capacitor Q is then calculated by [7]

$$\frac{1}{Q_c} = \frac{1}{Q_u} - \frac{1}{Q_r}. \quad (1)$$

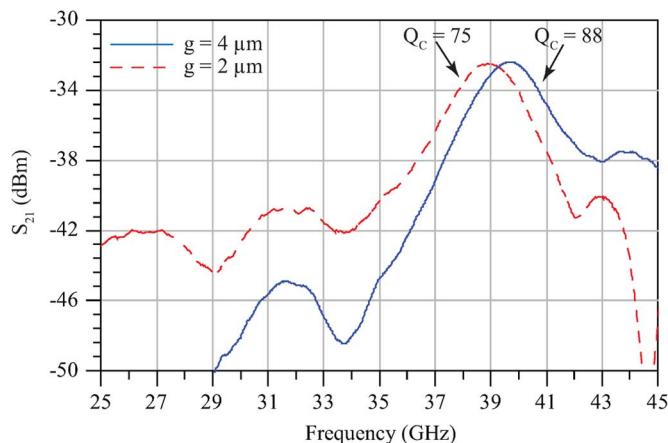


Fig. 15. Q -factor characterization for fabricated prototype of Design III: transmission measurements of a weakly coupled transmission-line resonator loaded with the tunable capacitor prototype of Design III.

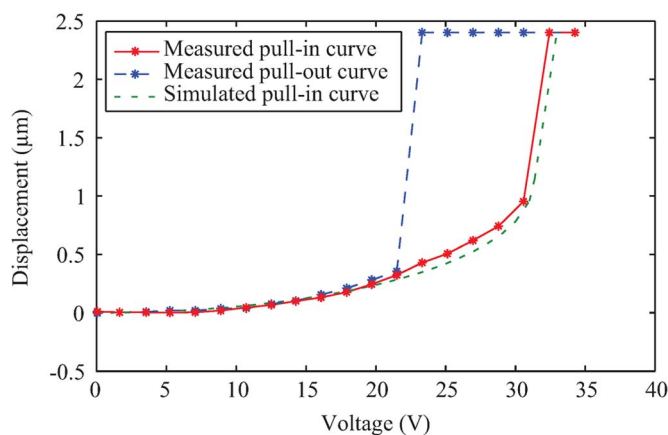


Fig. 16. Measured and simulated dc-actuation hysteresis of a prototype device of Design III with a spring constant of 5.8 N/m.

Fig. 15 shows the transmission measurement results of the weakly coupled resonator ($S_{21} < -20$ dB) loaded with a capacitor in the two extreme states. For the first measurement, the capacitor gap to the transmission line is $4 \mu\text{m}$ and the extracted Q_c is 88 at 40 GHz, and for the second measurement, the capacitor gap to the transmission line is $2 \mu\text{m}$, leading to an extracted Q_c of 75.

2) *Actuator Characterization*: All displacement measurements for actuation voltage, resonance frequency, self-actuation, and response time were performed using a Veeco Wyko NT9300 white-light interferometer, with the chip being placed in a slanting position underneath the lens of the profilometer. Fig. 16 shows the measured actuation and release curve for a tunable capacitor of Design III. Using COMSOL Multiphysics simulations with the measured dimensions of the fabricated geometry, a mechanical spring constant of 5.8 N/m was extracted. For the fabricated devices, the actuator moves by a total of $2.4 \mu\text{m}$ as compared to the nominal $2 \mu\text{m}$. The measured average pull-in voltage, for 20 cycle measurements, is 30.70 V with a standard deviation of 1.08 V. For the releases voltage, the average is 21.15 V with a standard deviation of 1.71 V. Fig. 16 shows the agreement of the measured displacement of a com-

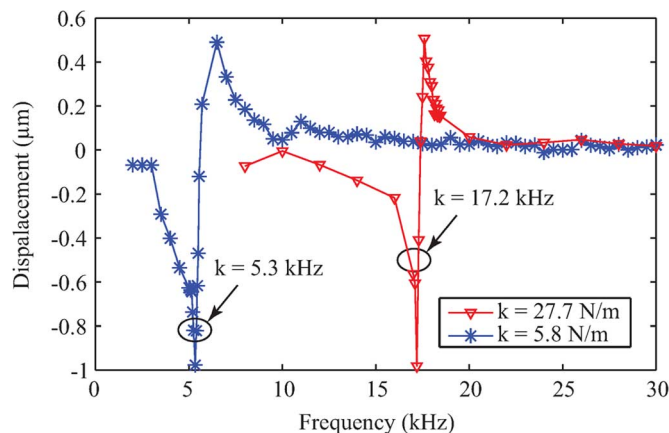


Fig. 17. Measurements of mechanical resonance frequencies for two prototype devices of Design III with spring constants of 5.8 and 27.7 N/m, using a white-light interferometer.

plete cycle with COMSOL Multiphysics simulations based on the measured fabricated geometry.

Fig. 17 shows the measured mechanical resonance responses of two fabricated devices of Design III with different spring constants. For a spring constant of 5.8 N/m, the mechanical resonance frequency was measured to be 5.3 kHz, and a spring constant of 27.7 N/m results in a mechanical resonance frequency of 17.2 kHz.

Multiple response curves of a device with a spring constant of 5.8 N/m were also measured to characterize the response time of the actuator, and are plotted in Fig. 18. When the actuator is pulled in, it shows characteristic bouncing behavior as shown in Fig. 18(a). The actuator pull-in time to the first bouncing event is $60 \mu\text{s}$, and the time for the actuator bouncing to drop below 8% of the gap is $140 \mu\text{s}$. Similarly, Fig. 18(b) shows the release time measurements of the same actuator. The release is followed by multiple oscillation events implying that there is very low damping of the unpackaged device. However, by packaging the device in an overpressure or high viscosity gas environment, critical damping ($Q = 0.5$) can be achieved, eliminating the ringing, and thus reducing the response time of the device [11]. A mechanical Q of 3.9 was extracted by curve fitting from the response curves. The oscillation frequency is in good agreement with the measured mechanical resonance frequency of the device.

3) *Power Handling, Linearity, and Reliability Characterization*: Even if the mechanical resonance frequency is several orders of magnitude lower than the RF signal frequency, a high RF power might cause self actuation. The effective signal voltage corresponds to an equivalent dc voltage on the moving sidewalls since the electrostatic force is proportional to the square of the signal voltage. The advantage of Design III over Design I and II is that there is an additional capacitor for coupling to the ground, which reduces the effective actuation force created by the signal voltage on the moving sidewalls. The self-actuation robustness was determined by applying a 60-kHz low-frequency power signal and the subsequent deflection was measured using a white-light interferometer. Two devices of Design III, having spring constants of 5.8 and 27.7 N/m, respectively, were measured for increasing power levels up to 50 dBm.

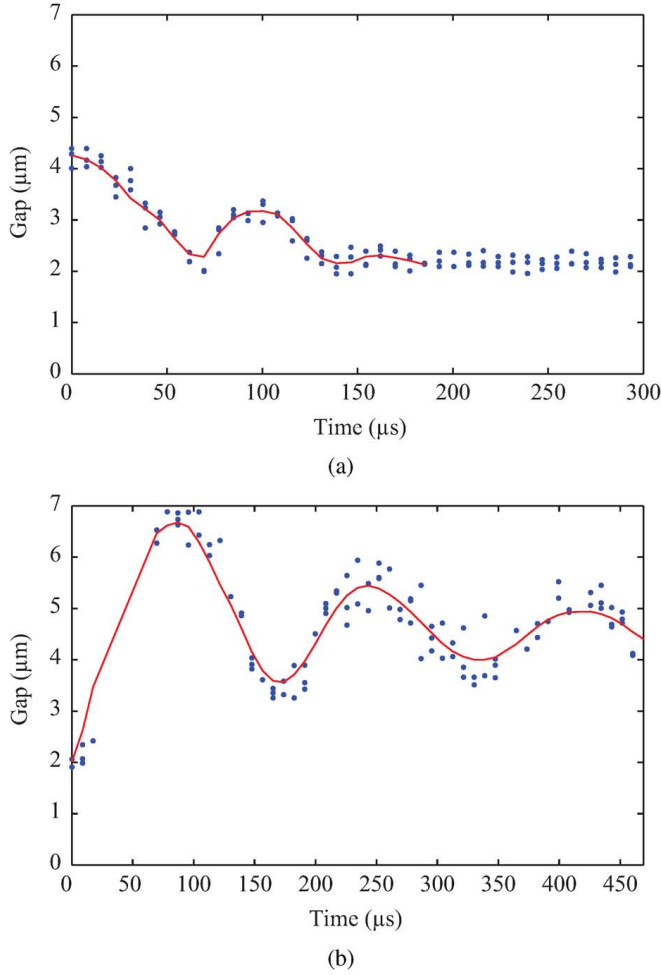


Fig. 18. Pull-in and pull-out transient measurements of multiple actuation events of a tunable capacitor of Design III ($k = 5.8$ N/m), measured with a white-light interferometer. (a) Pull-in and (b) release.

Fig. 19 shows that for the device with $k = 5.8$ N/m, self-actuation pull-in occurs at 41.5 dBm, and for the device with $k = 27.7$ N/m, self-actuation pull-in occurs at 47.8 dBm. The vicinity of the test RF frequency of 60 kHz to the mechanical resonance frequencies of 5.3 and 17.2 kHz for the devices with 5.8- and 27.7-N/m spring constants, respectively, stimulates an attenuated mechanical movement of the movable ground sidewalls, which attributes with an error to the self-actuation power measurement of less than 1% and less than 7% for the two spring designs, respectively. In principle, the stoppers of the actuator should limit the movement to the pull-in position, but it was noted that with high signal power levels of beyond 40 dBm, the moving sidewall can tilt, which frequently created a non-reversible short circuit to the signal line during the power-level tests. The theoretical self-actuation voltage was also calculated for comparison using the modified dc pull-in voltage relation describing the dc-equivalent self-actuation voltage between the signal line and a single moving sidewall

$$V_P = \sqrt{\frac{8kg_o^2}{27C_o}} \quad (2)$$

where the spring constant k is 5.8 and 27.7 N/m for the two design implementations, respectively, the initial gap g_o is 4.4 μm

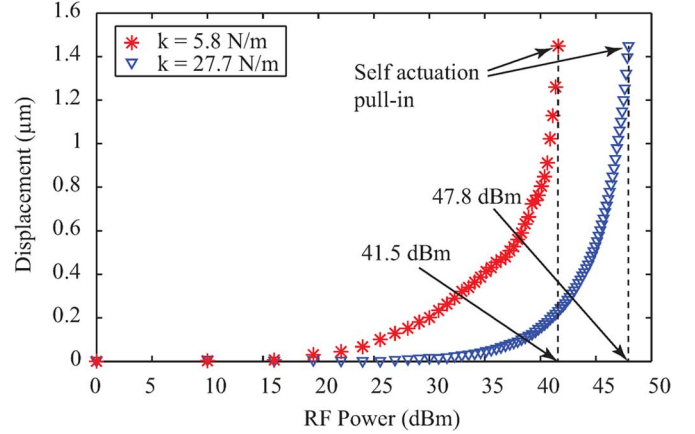


Fig. 19. Measurement of self-actuation behavior using a 60-kHz high-power signal on the RF transmission line, on two prototype devices of Design III with spring constants of 5.8 and 27.7 N/m, using a white-light interferometer.

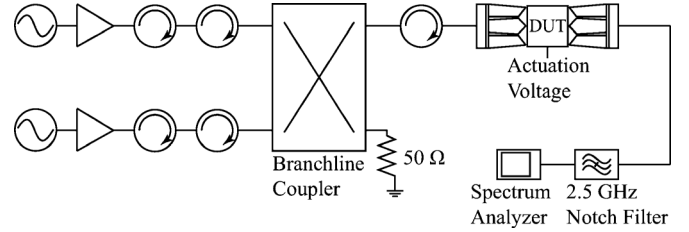


Fig. 20. Two-tone intermodulation distortion measurement setup.

and the capacitor value C_o between the signal line and a single moving sidewall is 46.2 fF. V_P is then calculated to be 26.84 V ($k = 5.8$ N/m) and 58.65 V ($k = 27.7$ N/m). The necessary total voltage between the signal line and the RF ground for self-actuation is then calculated by reversing the voltage division between the signal line capacitor C_o and the overall coupling capacitor C_c for a single sidewall: $V_{\text{RMS}} = V_P(C_c + C_o)/C_c$. The calculated values are 62 and 135.48 V for the 5.8 and 27.7 N/m spring designs, respectively, which are equivalent to the self-actuation pull-in power levels 48.86 and 55.65 dBm, respectively, which deviate by about 7 dB from the measured values.

The linearity characteristic was determined by measuring the two-tone third-order intermodulation intercept point (IIP3) with two signal sources and amplifiers at a center frequency of 2.5 GHz, separated by a 12-MHz offset. This offset frequency was chosen based on the availability of commercial notch filters with such a bandwidth at a 2.5-GHz center frequency. Such a notch filter is necessary in order not to overload the spectrum analyzer input [37]. Fig. 20 shows the two-tone IIP3 measurement setup using a notch filter ($f_0 = 2.5$ GHz, maximum passband insertion loss = 1.5 dB, rejection center >50 dBc from 2.4970 to 2.5070 MHz) for suppressing the two fundamental tones to avoid the influence of the nonlinearity of the spectrum analyzer itself. Furthermore, double isolators are used to avoid any nonlinearity of the power amplifiers having an adverse affect on the final IIP3 measurement, and to protect the amplifiers. The IIP3 measurements were carried out for all three states of a prototype device of Design III: unactuated, single-side (asymmetrically) actuated, and double-side (symmetrically) actuated. Fig. 21 shows that the IIP3 measurements

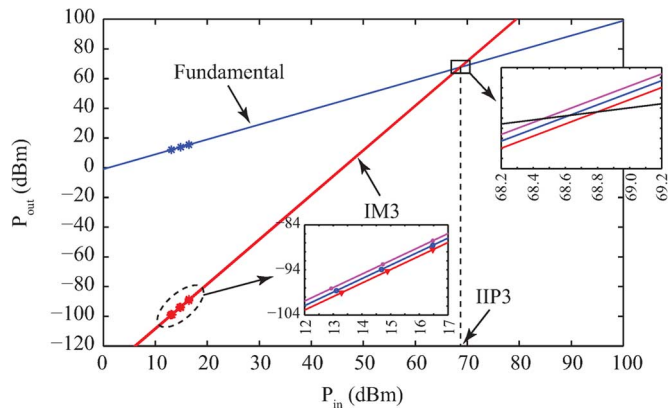


Fig. 21. Measured dual-tone fundamental and intermodulation levels versus input power for three states of a device of Design III ($f = 2.5$ GHz $\Delta f = 12$ MHz).

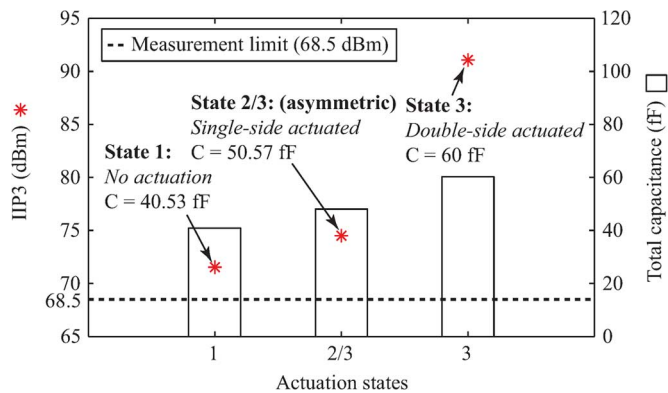


Fig. 22. Calculated IIP3 for the three states of a device of Design III ($f = 2.5$ GHz), derived from measured capacitances, the geometries of the fabricated device, and the simulated spring constants.

reach a common limit at 68.5 dBm for all the three states of the capacitor. This value was also found for an IIP3 measurement of a transmission line alone. Thus, it can be assumed that the measured nonlinearity is limited by the transmission line measurement setup, and not the MEMS device. Fig. 22 shows the calculated IIP3 for the device in the three different states at 2.5 GHz, derived from the measured capacitances, measured sidewall displacements, and simulated spring constants of the three states of the device using the following equation:

$$\text{IIP3} = \frac{4k_1g_1^2k_2g_2^2}{[\omega C_1^2(k_2g_2^2) + \omega C_2^2(k_1g_1^2)] Z_o^2} \quad (3)$$

where k_1 and k_2 are the spring constants of left- and right-side actuators, g_1 and g_2 are the capacitor gaps of each side, C_1 and C_2 are the capacitances of each side, Z_o is the characteristic impedance, and ω is the angular frequency. This equation for a double-side capacitance has been derived from the single capacitance equations $\text{IIP3} = 2k_1g_1^2/\phi C Z_o$, $\phi = -\omega C Z_o/2$ [7], where ϕ is the phase of the output signal.

The IIP3 of the three discrete states of the device have been determined as 71.4, 74.4, and 91.0 dBm. The spring constants utilized for these calculated IIP3 values were determined by simulating the device geometry with dimensions measured from the fabricated prototypes, which is 5.8 and 5650 N/m for the

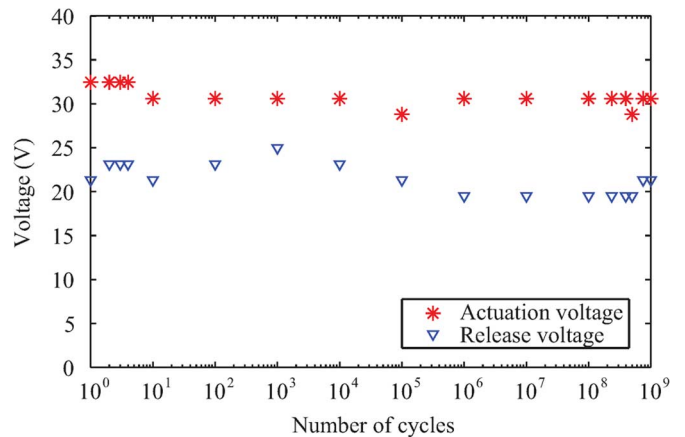


Fig. 23. Lifetime characterization: pull-in and pull-out voltages monitored over 1 billion cycles with 34-V unipolar square waveform with a 35% duty cycle and a cycle frequency of 1.6 kHz for a device with $k = 5.8$ N/m of Design III, determined by white-light interferometry for measuring the pull-in/pull-out actuation hysteresis for each data point (see Fig. 16).

nonactuated and actuated (i.e., electrostatically clamped) state, respectively. These IIP3 values are, for all states, well above the measurement limit found for our measurement setup, which confirms the indifference of the IIP3 of the three states measured with our setup. The increase in IIP3 with the increasing capacitance seems to be counterintuitive as compared to conventional MEMS capacitor designs. The increase in IIP3 is caused due to the increase in the spring constant when one side or both sides are actuated since they are electrostatically clamped upon actuation. The k values for Design III for one side is increased approximately by power of 5 from 5.8 to 5650 N/m when that side is actuated. The IIP3 equations derived above are valid for frequencies equal to or below the mechanical resonance frequencies and there is a further 40-dB/decade decrease of the intermodulation levels above the mechanical resonance frequency.

Lifetime measurements were performed on a tunable capacitor of Design III with a spring constant of 5.8 N/m (average actuation voltage of 30.7 V) in an uncontrolled atmospheric environment. The device was cycled with an actuation voltage of 34 V using a unipolar square waveform with a 35% duty cycle and a cycle frequency of 1.6 kHz. The pull-in and pull-out hysteresis curves were monitored after each decade of actuation cycles to derive the pull-in and pull-out voltages over the lifetime. The actuation and release voltage values averaged from three actuation cycles at each measurement point are shown in Fig. 23. After the first ten cycles, the actuation voltage remains constant at 30.5 V with little variation over the 1 billion cycles. The release voltage fluctuates more over the 1 billion cycles, eventually stabilizing at 19.5 V between 1–400 million cycles and moving up to 21.5 V between 500 million–1 billion cycles. The measurements were stopped after eight days with more than 22 h of accumulated pull-in time, when one billion cycles were reached without observing any failure, fatigue, or altered pull-in hysteresis. Neither the stoppers, nor other actuator elements showed any signs of wear when inspected in the SEM after the lifetime measurements. The lifetime characterization agrees very well with other silicon-core all-metal RF MEMS devices developed by the authors [38].

V. CONCLUSION

This paper has demonstrated the concept of a novel RF MEMS tunable capacitors based on moving ground sidewalls of 3-D micromachined coplanar transmission lines with integrated MEMS actuators. The device concept enables multiple tuning steps in discrete and well-defined positions. Embodiments of different device concepts were successfully demonstrated, achieving extraordinary high Q , high reliability, high linearity, and high self-actuation robustness at medium actuation voltages.

ACKNOWLEDGMENT

The authors would like to thank J. Åberg, MicroComp Nordic AB, Stockholm, Sweden, for his help with the nonlinearity measurement setup and for providing essential equipment. The authors also wish to thank A. Cheshire and G. Roupillard, Applied Materials, Stockholm, Sweden, for the SiO₂ and Si deep etching of some of the prototype devices on a Centura etching platform. Furthermore, the help of A. Fischer, KTH Royal Institute of Technology, Stockholm, Sweden, with wire bonding for measuring the prototypes, and of K. Noren, KTH Royal Institute of Technology, with the critical point dryer, is highly appreciated.

REFERENCES

- [1] H. Xu and K. K. O., "High- Q thick-gate-oxide MOS varactors with subdesign-rule channel lengths for millimeter-wave applications," *IEEE Electron Device Lett.*, vol. 29, no. 4, pp. 363–365, Apr. 2008.
- [2] Y. Oh and J.-S. Rieh, "A comprehensive study of high- Q island-gate varactors (IGVs) for CMOS millimeter-wave applications," *IEEE Trans. Microw. Theory Techn.*, vol. 59, no. 6, pp. 1520–1528, Jun. 2011.
- [3] C. Huang, P. J. Zampardi, K. Buisman, C. Cismaru, M. Sun, K. Stevens, J. Fu, M. Marchetti, and L. C. N. de Vreede, "A GaAs junction varactor with a continuously tunable range of 9:1 and an OIP3 of 57 dBm," *IEEE Electron Device Lett.*, vol. 31, no. 2, pp. 108–110, Feb. 2010.
- [4] N. Somjit, G. Stemme, and J. Oberhammer, "Binary-coded 4.25-bit W -band monocrystalline-silicon MEMS multi-stage dielectric-block phase shifters," *IEEE Trans. Microw. Theory Techn.*, vol. 57, no. 11, pp. 2834–2840, Nov. 2009.
- [5] A. Abbaspour-Tamijani, L. Dussopt, and G. M. Rebeiz, "Miniature and tunable filters using MEMS capacitors," *IEEE Trans. Microw. Theory Techn.*, vol. 51, no. 7, pp. 1878–1885, Jul. 2003.
- [6] Q. Shen and N. S. Barker, "Distributed MEMS tunable matching network using minimal-contact RF-MEMS varactors," *IEEE Trans. Microw. Theory Techn.*, vol. 54, no. 6, pp. 2646–2658, Jun. 2006.
- [7] G. M. Rebeiz, *RF MEMS Theory, Design, and Technology*. New York, NY, USA: Wiley, 2003.
- [8] L. Dussopt and G. M. Rebeiz, "High- Q millimeter-wave MEMS varactors: Extended tuning range and discrete-position designs," in *IEEE MTT-S Int. Microw. Symp. Dig.*, 2002, pp. 1205–1208.
- [9] B. Lacroix, A. Pothier, A. Crunteanu, C. Cibert, F. Dumas-Bouchiat, C. Champeaux, A. Catherinot, and P. Blondy, "Sub-microsecond RF MEMS switched capacitors," *IEEE Trans. Microw. Theory Techn.*, vol. 55, no. 6, pp. 1314–1321, Jun. 2007.
- [10] A. Grichener, D. Mercier, and G. M. Rebeiz, "High-power high-reliability high- Q switched RF MEMS capacitors," in *IEEE MTT-S Int. Microw. Symp. Dig.*, Jun. 2006, pp. 31–34.
- [11] R. L. Borwick, III, P. A. Stupar, J. F. DeNatale, R. Anderson, and R. Erlanson, "Variable MEMS capacitors implemented into RF filter systems," *IEEE Trans. Microw. Theory Techn.*, vol. 51, no. 1, pp. 315–319, Jan. 2003.
- [12] K. Entesari, K. Obeidat, A. R. Brown, and G. M. Rebeiz, "A 25–75 MHz RF MEMS tunable filter," *IEEE Trans. Microw. Theory Techn.*, vol. 55, no. 11, pp. 2399–2405, Nov. 2007.
- [13] K. Entesari and G. M. Rebeiz, "A differential 4-bit 6.5–10 GHz RF MEMS tunable filter," *IEEE Trans. Microw. Theory Techn.*, vol. 53, no. 3, pp. 1103–1110, Mar. 2005.
- [14] T.-Y. Yun and K. Chang, "A low-loss time-delay phase shifter controlled by piezoelectric transducer to perturb microstrip line," *IEEE Microw. Guided Wave Lett.*, vol. 10, no. 3, pp. 96–98, Mar. 2000.
- [15] N. Somjit, G. Stemme, and J. Oberhammer, "Power handling analysis of high-power W -band all-silicon MEMS phase shifters," *IEEE Trans. Electron Devices*, vol. 58, no. 5, pp. 1548–1555, May 2011.
- [16] A. S. Morris, Q. Gu, M. Ozkar, and S. P. Natarajan, "High performance tuners for handsets," in *IEEE MTT-S Int. Microw. Symp. Dig.*, Jun. 2011, pp. 1–4.
- [17] B. Lakshminarayan, D. Mercier, and G. M. Rebeiz, "High-reliability miniature RF-MEMS switched capacitors," *IEEE Trans. Microw. Theory Techn.*, vol. 56, no. 4, pp. 971–981, Apr. 2008.
- [18] L. Dussopt and G. M. Rebeiz, "An X - to K -band 3-bit digital MEMS varactor," *IEEE Microw. Wireless Compon. Lett.*, vol. 13, no. 9, pp. 361–363, Sep. 2003.
- [19] A. Grichener and G. M. Rebeiz, "High-reliability RF-MEMS switched capacitors with digital and analog tuning characteristics," *IEEE Trans. Microw. Theory Techn.*, vol. 58, no. 10, pp. 2692–2701, Oct. 2010.
- [20] M. Bakri-Kassem, S. Fouladi, and R. R. Mansour, "Novel high- Q MEMS curled-plate variable capacitors fabricated in 0.35- μ m CMOS technology," *IEEE Trans. Microw. Theory Techn.*, vol. 56, no. 2, pp. 530–541, Feb. 2008.
- [21] M. Bakri-Kassem and R. Mansour, "Two movable-plate nitride-loaded MEMS variable capacitor," *IEEE Trans. Microw. Theory Techn.*, vol. 52, no. 3, pp. 831–837, Mar. 2004.
- [22] I. Reines, B. Pillans, and G. M. Rebeiz, "Thin-film aluminum RF MEMS switched capacitors with stress tolerance and temperature stability," *J. Microelectromech. Syst.*, vol. 20, no. 1, pp. 193–203, Feb. 2011.
- [23] J. Reinke, G. K. Fedder, and T. Mukherjee, "CMOS-MEMS 3-bit digital capacitors with tuning ratios greater than 60:1," *IEEE Trans. Microw. Theory Techn.*, vol. 59, no. 5, pp. 1238–1248, May 2011.
- [24] C. M. Andersson, N. Ejebjrk, A. Henry, S. Andersson, E. Janzn, H. Zirath, and N. Rorsman, "A SiC varactor with large effective tuning range for microwave power applications," *IEEE Electron Device Lett.*, vol. 32, no. 6, pp. 788–790, Jun. 2011.
- [25] "PE64904 5-bit 32-state digitally tunable capacitor," Peregrine Semiconductor, San Diego, CA, USA, 2011–2012.
- [26] M. Sterner, N. Roxhed, G. Stemme, and J. Oberhammer, "Static zero-power-consumption coplanar waveguide embedded DC-to-RF metal-contact MEMS switches in two-port and three-port configuration," *IEEE Trans. Electron Devices*, vol. 57, no. 7, pp. 1659–1669, Jul. 2010.
- [27] U. Shah, M. Sterner, G. Stemme, and J. Oberhammer, "RF MEMS tuneable capacitors based on moveable sidewalls in 3-D micromachined coplanar transmission lines," in *Proc. Asia-Pacific Microw. Conf.*, Mar. 2011, pp. 1821–1824.
- [28] U. Shah, M. Sterner, G. Stemme, and J. Oberhammer, "Multi-position large tuning-range digitally tuneable capacitors embedded in 3-D micromachined transmission lines," in *IEEE Int. Microelectromech. Syst. Conf.*, Mar. 2011, pp. 165–168.
- [29] U. Shah, M. Sterner, and J. Oberhammer, "Basic concepts of moving-side-wall tunable capacitors for RF MEMS reconfigurable filters," in *Proc. Eur. Microw. Conf.*, Dec. 2011, pp. 1087–1090.
- [30] Z. Peng, X. Yuan, J. C. M. Hwang, D. I. Forehand, and C. L. Goldsmith, "Superposition model for dielectric charging of RF MEMS capacitive switches under bipolar control-voltage waveforms," *IEEE Trans. Microw. Theory Techn.*, vol. 55, no. 12, pp. 2911–2918, Dec. 2007.
- [31] I. L. Garro and A. C. Chavez, "Micromachined transmission lines for millimeter-wave applications," in *Proc. Int. CONIELECOMP Conf.*, Feb. 2006, pp. 15–20.
- [32] R. N. Simons, *Coplanar Waveguide Circuits, Components, and Systems*. New York, NY, USA: Wiley, 2001.
- [33] I. Wolff, *Coplanar Microwave Integrated Circuits*. Hoboken, NJ, USA: Wiley, 2006.
- [34] M. Sterner, N. Roxhed, G. Stemme, and J. Oberhammer, "Electrochemically assisted maskless selective removal of metal layers for three-dimensional micromachined SOI RF MEMS transmission lines and devices," *J. Microelectromech. Syst.*, vol. 20, no. 4, pp. 899–908, Aug. 2011.
- [35] Z. Hu and T. Ritzdorf, "Cyanide- and thiourea-free electrochemical etching of gold for microelectronics applications," *J. Electrochem. Soc.*, vol. 154, no. 10, pp. D543–D549, Aug. 2007.
- [36] M. H. Cho, G. W. Huang, K. M. Chen, and A. S. Peng, "A novel cascade-based de-embedding method for on-wafer microwave characterization and automatic measurement," in *IEEE MTT-S Int. Microw. Symp. Dig.*, Jun. 2004, pp. 1237–1240.

- [37] C. Patel and G. M. Rebeiz, "A high-reliability high-linearity high-power RF MEMS metal-contact switch for DC-40-GHz applications," *IEEE Trans. Microw. Theory Techn.*, vol. 60, no. 10, pp. 3096–3112, Oct. 2012.
- [38] M. Sterner, N. Somjit, U. Shah, S. Dudorov, D. Chicherin, A. Raisanen, and J. Oberhammer, "Microwave MEMS devices designed for process robustness and operational reliability," *Int. J. Microw. Wireless Technol.*, vol. 3, no. 5, pp. 547–563, Oct. 2011.



Umer Shah (S'09) was born in Bannu, Pakistan, in 1981. He received the B.S. degree in engineering from the GIK Institute, Topi, Pakistan, in 2003, and the Masters of Science degree in wireless engineering (with an emphasis on RF integrated circuits (RFICs), monolithic microwave integrated circuits (MMICs), and antenna design) from the Technical University of Denmark (DTU), Copenhagen, Denmark, in 2007.

He spent one year as a Researcher with the GIK Institute prior to earning the Masters in Science degree.

His Masters thesis research was with Interactive Sports Games (ISG) A/S. Following the Masters of Science degree, he was involved with the development of satellite front ends with a research organization. Since December 2008, he has been a Ph.D. student with the MST Group, KTH Royal Institute of Technology, Stockholm, Sweden. His research focus includes RF MEMS-based filters, phase shifters, matching circuits, and antennas. His further interests includes MMICs, RFICs, and antenna design.

Mr. Shah was the recipient of the Best Student Paper Award presented at the 2010 Asia–Pacific Microwave Conference, Yokohama, Japan.



Mikael Sterner was born in Stockholm, Sweden, in 1981. He received the M.Sc. degree in engineering physics from the KTH Royal Institute of Technology, Stockholm, Sweden, in 2006, and is currently working toward the Ph.D. degree in microsystems technology at the KTH Royal Institute of Technology.

Since 2006, he has been with the Microsystem Technology Laboratory, KTH Royal Institute of Technology. His main research fields are RF MEMS switches and microwave MEMS tunable

high-impedance surfaces.



Joachim Oberhammer (M'06–SM'12) was born in Brunico, Italy, in 1976. He received the M.Sc. degree in electrical engineering from the Graz University of Technology, Graz, Austria, in 2000, and the Ph.D. degree from the KTH Royal Institute of Technology, Stockholm, Sweden, in 2004. His doctoral research concerned RF MEMS switches and microsystem packaging.

He was involved with automotive sensor electronics and RF identification (RFID) systems with the Graz University of Technology, and the Vienna

University of Technology, Vienna, Austria, prior to joining the Microsystem Technology Laboratory, KTH Royal Institute of Technology, Stockholm, Sweden. After having been a Post-Doctoral Research Fellow with the Nanyang Technological University, Singapore, he returned to the KTH Royal Institute of Technology in 2005, as an Assistant Professor. In 2007, he became an Associate Professor with the KTH Royal Institute of Technology, where he heads a research team with activities in RF and microwave MEMS. In 2007, he was a Research Consultant with the Nanyang Technological University. In 2008, he spent seven months as a Guest Researcher with Kyoto University, Kyoto, Japan. He has authored or coauthored over 50 reviewed research papers. He holds four patents.

Dr. Oberhammer was a TPRC member of IEEE Transducers (2009), the IEEE Microwave Theory and Techniques Society (IEEE MTT-S) International Microwave Symposium (IMS) (2010–2012), and the IEEE Microelectromechanical Systems (2011 and 2012). Since 2009, he has been a Steering Group member of the IEEE MTT-S and Antennas and Propagation (AP-S) Chapters Sweden. He was the recipient of the 2004 and 2007 Ericsson Research Foundation Award and a Swedish Innovation Bridge grant, respectively. He was the recipient of the 2008 Visiting Researcher Scholarship of the Japanese Society for the Promotion of Science. The research he heads was bestowed the Best Paper Award of the IEEE European Microwave Integrated Circuit Conference (2009), a Best Student Paper Award of the IEEE Asia–Pacific Microwave Conference (2010), and a Graduate Fellowship Award of the IEEE MTT-S (2010 and 2011).